Hard-sphere dispersions: Small-wave-vector structure-factor measurements in a linear shear flow

Bruce J. Ackerson,* Jos van der Werff, and C. G. de Kruif
Van 't Hoff Laboratorium, Rijksuniversiteit Utrecht, NL-3508 TB Utrecht, The Netherlands
(Received 22 October 1987)

Small-scattering-wave-vector structure-factor measurements have been made for model hard-sphere suspensions undergoing a steady linear shear flow. The samples are comprised of sterically stabilized silica particles in cyclohexane and have been well characterized previously by rheological, light scattering, and neutron scattering measurements. These combined measurements provide a strict test of recent theories of microscopic order in suspensions undergoing shear and suggest a picture which unifies several intuitive notions about suspensions undergoing shear flow: distortion of the pair correlation function, clustering, layering, and nonequilibrium phase transitions.

I. INTRODUCTION

The enormous success of statistical mechanics, in relating equilibrium microstructure to macroscopic properties and phase transitions, has been paralleled by a similar search for connections between microstructure and macroscopic properties in nonequilibrium systems. One area of active research is the relation of rheological properties to microscopic particle order in pure fluids and in particle suspension undergoing shear flow.[1,2] In pure-fluid systems the studies have mostly been done by molecular dynamics[3–5] (computer simulations) because the structural relaxation times are rapid (picoseconds) and shear rates must compete with these times (10^{12} sec^{-1}) to have observable effects. One exception to this rule is the shear-induced structural changes seen in binary liquid mixtures near the critical mixing point.[6,7] Here, of course, the structural relaxation times are greatly slowed and modest shear rates produce observable effects. In the molecular-dynamics studies the expected shear-induced distortion of the pair correlation function has been observed,[3,8–11] as well as transitions to more ordered quasisolid or liquid crystalline phases.[12–16] These structures include the formation of particle layers with the shear direction normal to the layers and the formation of strings of particles parallel to the velocity direction which are closely packed in a plane normal to the velocity. These structural changes produce highly non-Newtonian behavior, even in systems where the interparticle interaction is spherically symmetric.[17] Care must be exercised, however, because the methods used to control the temperature of the system may introduce artifacts.[18] Thus it is unfortunate that experimental verification of these phenomena is so difficult.

Alternatively, colloidal suspensions provide another class of systems with which to study similar nonequilibrium phenomena. Here the large-particle overdamped or diffusive dynamics is sufficiently slow that experiments are easily performed. In dense colloidal suspensions sliding layer structures have been observed.[19,20] The breakup of these layers has been associated with a shear thickening transition.[19,21] Ordering into layers has been reported for semidilute charge-stabilized systems,[22] but this may be associated with cell-surface ordering effects.[23] Dilute and semidilute charge-stabilized suspensions, which organize, respectively, into body-centered-cubic and face-centered-cubic structures in equilibrium, undergo a series of structural changes as the systems are "shear melted" by increasing the shear rate.[23–26] These structures include a flowing crystal, sliding layer, string, and amorphous ordering of particles. A close-packing criterion for the melting order is followed.

While organization into layers is observed in "dense" systems (e.g., systems which are solid or glasses at rest), the notion is often employed to explain the shear thinning transition observed[19,21,22,27,28] in many systems. Here it is felt that Brownian motion at low shear rates keeps the system disordered; at larger shear rates hydrodynamic or direct interaction effects organize the system into a sliding layer structure, which reduces the measured shear viscosity. However, there are relatively few measurements made on shear-induced structures for systems which are known to have interparticle fluidlike order in equilibrium.[29,30] Conversely, a number of theories have been developed which predict viscosities and interparticle order in such systems. Surprisingly the theories predict only weak ordering or even a disordering with increasing shear rate. These theories described below should be tested.

In addition to the direct interparticle interaction in suspensions, the solvent introduces hydrodynamic and Brownian-motion effects. Most of the current theories for structure and viscosity include Brownian motion but may or may not include the interparticle hydrodynamic interactions. The viscosity theory of Beenakker and Mazur[31] neglects Brownian motion, but takes the hydrodynamic interaction between an arbitrary number of spheres into account.[32] The shear-induced structural distortion theories of Ronis[33(a),33(b)] and of Schwartzl and Hess[34(a),34(b)] neglect hydrodynamic interactions but include general interparticle potentials and Brownian motion. These theories make steady-state scattered-intensity predictions in terms of the static structure factor[35] $S(\mathbf{k})$ for a full range of shear rates and particle con-

centrations. On the other hand, Batchelor[36] has made detailed and intuitive calculations for both the structure in terms of the radial distribution function $g(\mathbf{r})$ (Ref. 35) and the viscosity of hard-sphere suspensions. These calculations include Brownian motion, direct interactions, and hydrodynamic interactions, but are limited to small shear rates and volume fractions. These calculations have been extended by Russel and Gast[37] using a potential of mean force approximation and a two-particle hydrodynamic interaction approximation to predict behavior at larger volume fractions.

At low shear rates most theories are analytic in the rate of shear and predict $S(\mathbf{k})$ directly[25,33(b),34(b)] or indirectly through $g(\mathbf{r})$ (Refs. 36 and 37) to have the following form:

$$S(\mathbf{k})=S_0(\mathbf{k})[1+k_x k_y \gamma A(\mathbf{k},\phi)] . \quad (1.1)$$

Here $S(\mathbf{k})$ is a generalization of the equilibrium static structure factor and represents a Fourier inversion of the nonequilibrium radial distribution function $g(\mathbf{r})$. It is a function of scattering wave vector $\mathbf{k}$, particle volume fraction ϕ, and rate of shear γ. $S_0(\mathbf{k})$ is the equilibrium structure factor, where x designates the flow velocity direction, y designates the shear direction, and A is a function of $\mathbf{k}$ and ϕ. The functional form of A depends on the theory being discussed. Thus it is possible, in principle, to make direct comparisons between light scattering measurements of $S(\mathbf{k})$ and the various theoretical predictions for $A(\mathbf{k},\phi)$ at sufficiently low rates of shear.

Computer simulations have also been used to investigate suspension behavior. Woodcock suggests direct application of damped Newtonian molecular dynamics[38] to suspensions. His calculations,[13] which neglect interparticle hydrodynamic interactions, indicate a shear-rate-dependent, nonequilibrium phase behavior. Here it is suggested that colloidal suspensions, which exhibit liquidlike or amorphous interparticle ordering in equilibrium and at low shear rates, exhibit smectic or layering order at large rates of shear. The pure amorphous and pure smectic regions are separated by a finite range of shear rates where both phases coexist. This coexistence region extrapolates to zero shear and zero width as the equilibrium freezing transition is approached from low volume fractions. The coexistence region is also associated with the rheological shear thinning region. Similarly suspension-dynamics calculations for hard disks in two dimensions, which neglect Brownian motion but keep hydrodynamic interactions, find a distortion in the local colloidal particle order, particle clustering, and particle layering phenomena.[39] Particle clustering has been proposed as an important mechanism for increasing the shear viscosity at moderate volume fractions.[40]

The microscopic structural changes which give rise to shear thinning behavior remain clouded. The experimentally observed layering in concentrated systems, which exhibit shear thickening, suggests strong ordering effects. Yet systems which crystallize in equilibrium have also been shown to shear melt, to decrease their order with increasing shear rate. For systems which have liquidlike order in equilibrium, the computer simulations suggest a weak ordering or a distortion of the liquidlike order at low rates of shear followed by strong ordering of particles into strings, layers, or smectic structures at large rates of shear. On the other hand, analytic theories, which exhibit distortion of the liquidlike order at low rates of shear, indicate a decrease in overall order at large rates of shear.

Model colloidal systems exist which have liquidlike order in equilibrium and which exhibit a shear thinning transition. The associated microscopic order is not known. Do these systems exhibit "weak" or "strong" ordering with increasing shear rate? What is the degree of distortion of the equilibrium pair correlation function? Are string or layer phases formed? In an effort to address some of these questions, we have performed small-wave-vector static structure-factor measurements on such model hard-sphere suspensions. These measurements probe the "long"-wavelength shear-induced distortions of the pair correlation function for the colloidal particles, or in other terms, the nonequilibrium compressibility of the macroparticle system. Measurements were made for a broad range of shear rates and volume fractions. The spheres are well characterized by light and neutron scattering, and the rheological properties of the same suspensions have been determined.[41,42] These measurements prove to be very useful in answering many but not all of the questions asked above. In the following sections we discuss the experimental details, then results are presented and are followed by a discussion and conclusions.

II. EXPERIMENTAL DETAILS

A. Mechanical construction

A mechanical drawing of the parallel-plate shear cell employed in this experiment is presented in Fig. 1. The rotating disk (R) is an optical flat of radius 5 cm. The upper and lower cell surfaces are round glass plates of slightly larger radii. All three plates are commercially available windows obtained from Melles Griot. A conical adapter (as used in milling machines) is glued to the rotating plate at one end and fixed to a belt-driven gear box at the other. A small trough is glued to the top plate. When it is filled with water and the Teflon cap (S) is immersed, the cell is effectively sealed against evaporation losses.[42] The sample is contained and sheared in the gap (G) between the rotating plate and stationary bottom plate. The sample volume required to fill this gap is nominally 8 cm^3. It is introduced and withdrawn through a small hole drilled in the center of the bottom plate. The rotating plate, gear box, and stepping motor (M) can be moved vertically as a single unit. With the help of two high precision spindles and "rollers," the position of the upper assembly can be adjusted reproducibly with micrometer precision. Uniformity of gap spacing is critical and controlled by adjustment screws (A). Alignment is achieved using a small auxiliary laser directed along *CD* in Fig. 1 and by making adjustments so that all reflected beams from the glass plates are coincident and colinear. Any deviations from colinearity are due to lack of parallelism in the rotor (R) plate. The advantage of this shear cell is the ability to adjust the gap. This is important in defining the scattering volume and testing for boundary

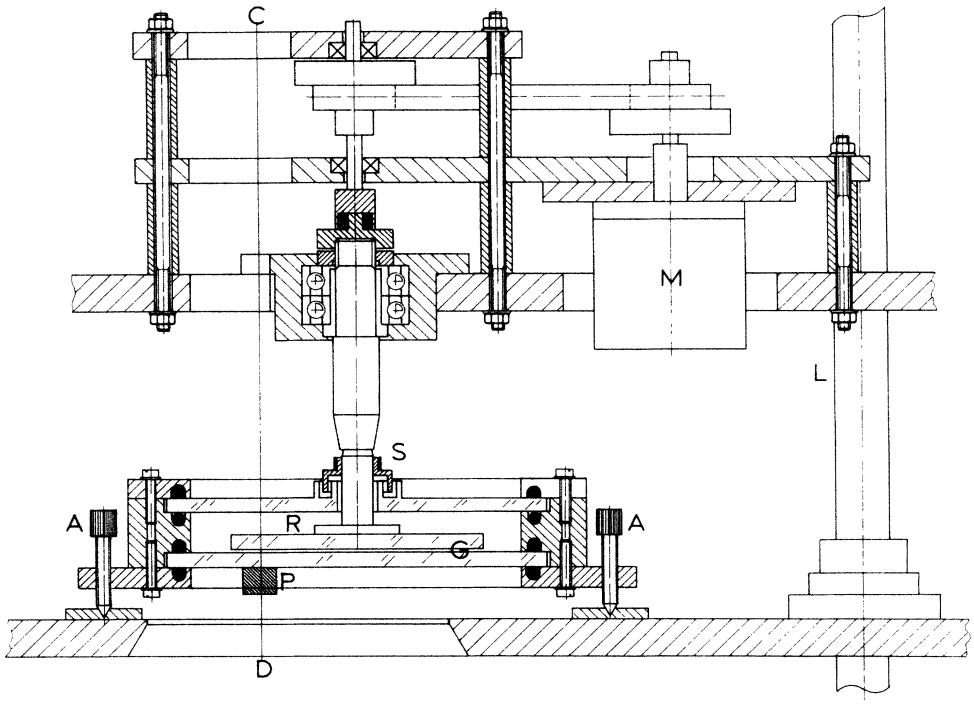

FIG. 1. Diagram of the sample cell. Here (A) is an adjustment to bring cell bottom parallel to rotating plate (R). (L) is one of four precision guide shafts for controlled motion of the upper carriage to adjust the cell gap (G) spacing. The seal (S) is filled with a non-volatile liquid to prevent sample evaporation and allows motion of the upper carriage to set the gap without disturbing the seal. (M) is the stepping motor. (P) is a prism for coupling the incident laser beam into the sample. The incident and collected light lie in the shear-velocity plane, which is normal to the plane of the page and parallel to *CD*.

layers. However, there is limited optical access and the cell gap must remain horizontal. We also have available a quartz couette cell.

B. Optics and detection

The scattering geometry is shown in Fig. 2. The plane of this figure is normal to the plane of Fig. 1 at the position CD. The incident laser beam ($\lambda = 6328$ Å) is directed normal to the surface of an isoceles prism which couples the beam into the gap containing the sample. The incident beam continues through the sample and is totally internally reflected by the rotating plate out of view of the detection optics. The scattering volume is determined by a 1-mm stop placed on the upper glass plate and another 1-mm stop positioned approximately 50 cm from the scattering volume. Both stops are positioned to determine one of two scattering angles (θ_1 and θ_2) with respect to the incident beam in the sample. The scattering volume is also viewed through the detection optics and is adjusted to be nearer to the lower stationary plate than the rotating plate. The important scattering parameters are the scattering wave vectors $\mathbf{k}_1$ and $\mathbf{k}_2$, which are each the difference between a scattered wave vector ($\mathbf{k}_{s1}$ or $\mathbf{k}_{s2}$) and the incident wave vector ($\mathbf{k}_I$). The scattering wave vectors lie in the shear-velocity plane, where the largest shear-induced distortion effects are expected. By reversing the direction of plate rotation two additional positions in k space may be examined as depicted in Fig. 3. The scattered light intensity is monitored by a photomultiplier (PM). This signal is electronically divided by the amplified signal from a photodiode which monitors the laser output intensity. The resulting signal is recorded on a chart recorder.

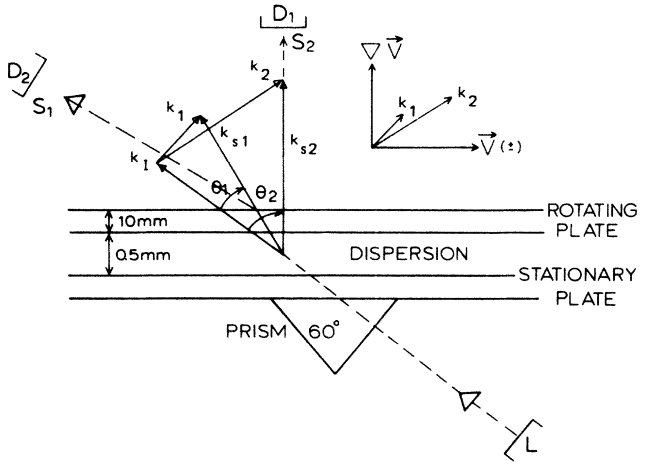

FIG. 2. Detailed view of the scattering volume in the shear-velocity plane. The incident (I) and scattered light paths (S_1) and (S_2) are indicated by dashed lines. (Note that the light paths are refracted mostly at the rotating plate-air interface.) The incident $\mathbf{k}_I$ and scattering wave vectors $\mathbf{k}_1 = \mathbf{k}_{s2} - \mathbf{k}_I$ and $\mathbf{k}_2 = \mathbf{k}_{s1} - \mathbf{k}_I$ are shown for the scattering angles θ_1 and θ_2 in the sample.

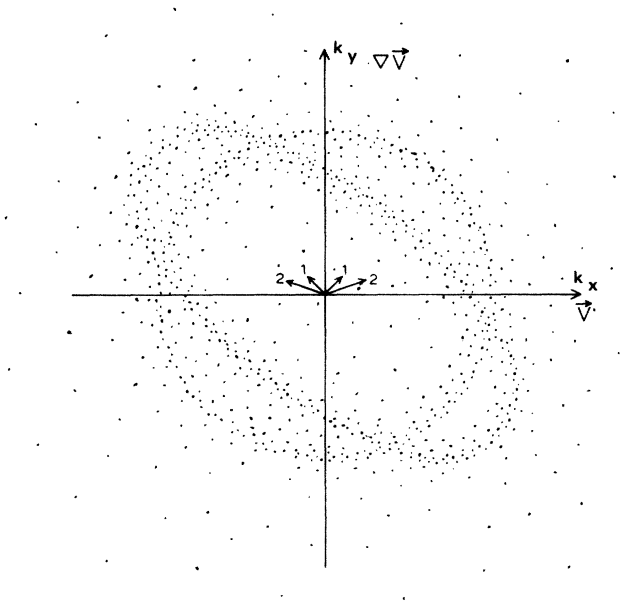

FIG. 3. Sketch of k-space structure in the shear-velocity plane. The ring (radius $\mathbf{k}_{DS} \cong \pi/a$) represents the position of the primary intensity maximum in the equilibrium colloidal particle static structure factor. The ellipse represents the expected distortion when the suspension is subjected to the linear shear indicated by $\nabla \mathbf{v}$ and $\mathbf{v}$. The vectors represent the positions in k space where experimental intensity data was collected. The lengths of these vectors ($k_1 = 0.7/a$ and $k_2 = 1.2/a$) are much less than $\mathbf{k}_{DS}$, indicating correlations over several particle diameters are being probed.

C. Samples

The samples used in these experiments are synthesized in our laboratory as described by van Helden.[43] They are suspensions of spherical silica particles sterically stabilized by octadecyl chains grafted to the particle surfaces. The solvent is cyclohexane, because it is a good solvent and has a refractive index ($n = 1.43$) which closely matches that of the particles ($n = 1.44$). The maximum turbidity occurs at a volume fraction $\phi \cong 0.13$ and decreases with increasing ϕ due to suppression of density fluctuations. The static (equilibrium) and dynamic (equilibrium fluctuation) properties have been studied and reported elsewhere.[44,45] The steady-state shear viscosity[42] and complex viscosity[41] have been measured for the same suspensions used in the experiments reported here. The earlier studies of these systems are well described by hard-sphere fluid theory. Therefore we view these suspensions as model hard-sphere systems.

Hard-sphere systems are expected to exhibit a freezing transition at $\phi \cong 0.494$ and a melting transition at $\phi \cong 0.545$. However, we have not observed crystallization in our samples. Because the mean particle radius is $a = 76$ nm and the polydispersity is $\sigma = 0.1$, crystallization may not be observed. The small particle radius means that any Bragg scattering of visible light will be backscattering or not physically possible. Alternatively, the polydispersity may be sufficiently large to frustrate crystallization. For the scattering angles and scattering wave vectors monitored in these experiments, collective particle order is examined. This corresponds to a small wave-vector limit where $|\mathbf{k}_{1,2}| \ll \pi/a$. Figure 3 indicates the magnitude of the scattering wave vector compared to the position of the Debye-Scherrer ring ($|\mathbf{k}_{DS}| \cong \pi/a$), the first intensity maximum in the static structure factor $S(\mathbf{k})$. Such measurements in the $\mathbf{k} \rightarrow 0$ limit correspond to equilibrium compressibility measurements or to generalized compressibility measurements in the case of an applied shear.

D. Data collection protocol and tests

After alignment of the cell and filling of the shear gap with the sample, we always adjusted the photodiode signal to the same level. The photomultiplier signal was also set to the same predetermined level by adjusting the high voltage. All other electronic adjustments are left the same. (Different settings did indicate linearity of the electronics.) The photomultiplier signal is divided by the photodiode signal and recorded on a chart recorder for several revolutions of the rotating disk in any given measurement. All measurements in a given run (at a given concentration ϕ) are frequently referenced to a predetermined shear rate and rotation direction to account for any systematic drifts during the run. The measured intensities at zero shear rate are then used to scale the data for a given run to the equilibrium intensity measurements determined in other experiments. Thus all intensity measurements in these experiments are *relative measurements* but are scaled to *absolute measurements* made previously.

Because intensity measurements are necessarily made through adjustable moving surfaces, we performed several experiments to test our apparatus. An aqueous suspension of submicron polystyrene spheres was diluted to have approximately the same maximum turbidity as seen in the silica suspensions. This very dilute sample ($\phi \cong 5 \times 10^{-4}$) exhibited no variation in scattered intensity as a function of shear rate and rotation direction. This expected result indicates good mechanical stability of the apparatus, even on reversal of the rotation direction. Intensity measurements at given volume fraction ϕ were repeated by each of the authors independently, at different times and for different loadings of the cell. The results were in agreement. There are no operator dependent artifacts. The micrometer measurement of the gap setting was checked by monitoring the scattered intensity as a function of gap setting. The measured intensity extrapolates to zero intensity at zero spacing. This result also indicates that boundary layer effects are not significant for the length scales in our experiments.

The shear rate can be varied by adjusting the stepping motor speed, changing the driving gear belt ratio, or changing the gap spacing. All the methods appeared to scale, indicating that results did not depend on mechanical properties of the apparatus. In the end all settings are referenced to a gap setting of 0.52 mm with the scattering volume 9.0 mm from the edge of the 50-mm-radius disk. At 1 rev s, this corresponds to a shear rate of $\gamma = 2\pi(41/0.52)\ \mathrm{s}^{-1} = 495\ \mathrm{s}^{-1}$.

III. RESULTS

Figures 4 and 5 present the logarithm of the scattered intensity versus the logarithm of the shear rate for scattering wave vectors $k_{1x}a=\pm 0.46$, $k_{1y}a=0.49$, $k_{1z}a=0.0$, and $k_{2x}a=\pm 0.97$, $k_{2y}a=0.64$, $k_{2z}=0.0$, respectively, where a is the particle radius. The shear rate γ is given in terms of the Péclet number, $N_{\mathrm{Pe}}=\gamma a^2/D_0=6\pi\eta_0 a^3\gamma/k_BT$, where D_0 is the free-particle diffusion constant, η_0 is the solvent viscosity, and k_BT is the thermal energy. The curves are parametrized by the particle volume fraction, which ranges from 0.06 to 0.55. The intensity measurements, which are relative values, as described in Sec. II, are scaled to the proper hard-sphere limit at zero shear for each volume fraction. This (polydisperse) hard-sphere value is given approximately by $\exp(-7.6\phi)$ and has been shown to fit previous absolute intensity measurements quite well.[46]

Measurements at these values of the scattering wave vector show systematic variation with increasing volume

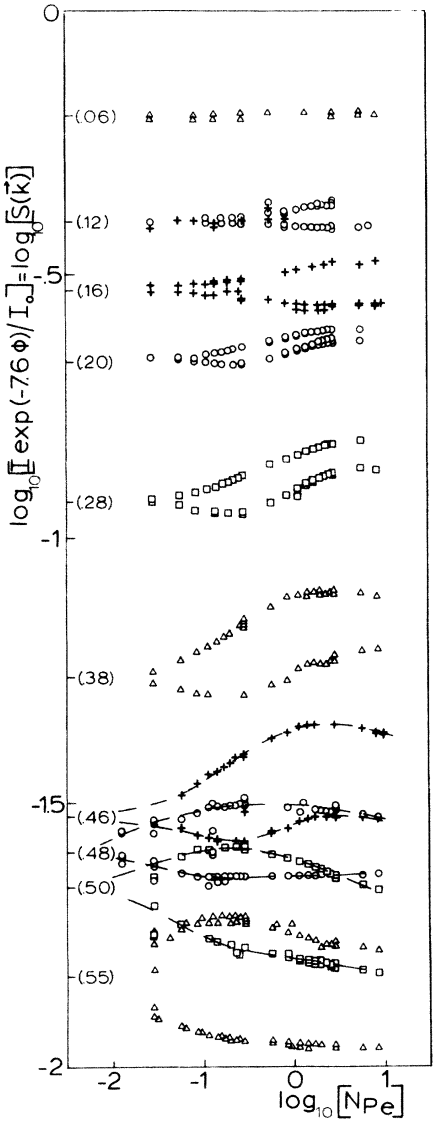

FIG. 4. Experimental results at $k_{1x}a=\pm 0.46$, $k_{1y}a=0.49$, $k_{1z}a=0.0$. Scattering intensities (I) are relative to scattering at zero shear rate (I_0). The data are brought to an approximate absolute scale by multiplying intensity by $\exp(-7.6\phi)$. This value represents the equilibrium osmotic compressibility. Volume fractions are indicated in parentheses. The horizontal axis represents the Péclet number $N_{\mathrm{Pe}}=\gamma a^2/D_0=6\pi\eta_0 a^3\gamma/kT$. Lines are drawn to guide the eye. Note that two independent experiments were done with samples with $\phi=0.12$. The circles and crosses give the data points for the two independent experiments.

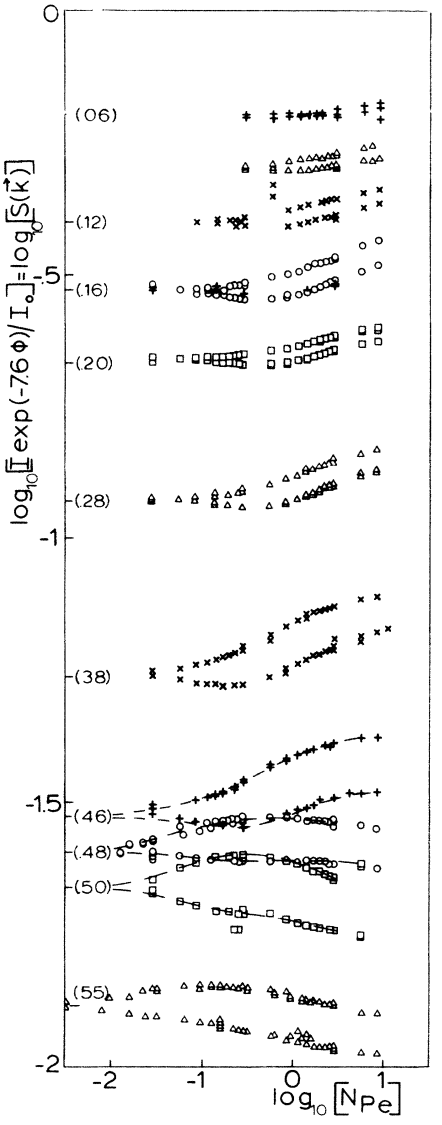

FIG. 5. Experimental results at $k_{2x}a=\pm 0.97$ and $k_{2y}a=0.64$, $k_{1z}a=0.0$. Scattering intensities (I) are relative to scattering at zero shear rate (I_0). The data are brought to an approximate absolute scale by multiplying intensity by $\exp(-7.6\phi)$. This value represents the equilibrium osmotic compressibility. Volume fractions are indicated in parentheses. The horizontal axis represents the Péclet number $N_{\mathrm{Pe}}=\gamma a^2/D_0=6\pi\eta_0 a^3\gamma/kT$. Lines are drawn to guide the eye. Note that two independent experiments were done with samples with $\phi=0.16$. The circles and crosses give the data points for the two independent experiments.

fraction and shear rate. At low shear rates the measurements for $k_x > 0$ increase with increasing shear rate, while measurements for $k_x < 0$ decrease with increasing shear rate. This behavior is in accord with the expected distortion of the static structure factor at low shear rates, as depicted in Fig. 3. In this figure the primary maximum in the equilibrium static structure factor $S_0(\mathbf{k})$ is represented by the circle (of radius $k \cong \pi/a$ for hard spheres of radius a) in the k_x-k_y plane. The low-shear-rate distorted $S(\mathbf{k})$ given in Eq. (1.1) is represented by the ellipse in Fig. 3. The shift in the primary maximum in $S(\mathbf{k})$ depends on the direction $\mathbf{k}$ to produce an elliptical shape, and the magnitude of $S(\mathbf{k})$ may vary from point to point on the ellipse. The vectors in Fig. 3 represent the different scattering-wave-vector positions at which $S(\mathbf{k})$ was monitored in our experiments. When the ellipse collapses toward the origin along the $k_v = k_{\nabla v}$ line, the intensities near the origin are expected to increase along the same direction. Conversely, when $S(\mathbf{k})$ is measured along the $k_v = -k_{\nabla v}$ line, the values are expected to decrease as the maximum in $S(\mathbf{k})$ moves outward with increasing rate of shear. However, this systematic behavior does not continue indefinitely with increasing shear. At a certain shear rate, which depends on the volume fraction, the decreasing intensity reaches a minimum and then increases. The intensities for both $k_x > 0$ and $k_x < 0$ now increase at roughly the same rate with increasing shear rate. Then the upper intensity reaches a maximum and begins to decrease with the lower intensity following suit.

The variation in intensity with increasing shear rate scales to smaller rates of shear as the volume fraction increases and is at slightly different rates of shear in Figs. 4 and 5. At the hard-sphere freezing transition (volume fraction equal to 0.494) little variation is seen except the initial splitting of the $k_x > 0$ and $k_x < 0$ intensities. For larger volume fractions the $k_x > 0$ and $k_x < 0$ intensities split as before but are followed by a decrease in both intensities with increasing shear rate. A "phase diagram" has been constructed in Fig. 6 from the data in Fig. 4 by determining the minimal position in the $k_x < 0$ data and the maximal position of the $k_x > 0$ data and plotting these shear rates as a function of the corresponding volume fraction. A similar (but not identical, see Fig. 7) plot results for the data from Fig. 5. This phase diagram shows that the shear rates producing maximal and minimal intensities are well separated at low volume fraction but converge to the same low-shear-rate value at the hard-sphere freezing volume fraction. Also plotted is the characteristic shear rate, where the reduced shear viscosity is halfway between its limiting Newtonian large viscosity low-shear-rate value and its small viscosity high-shear-rate value.[42] It is seen that these shear-rate values are bounded by the maximal and minimal values and also converge to the same shear rate at the freezing transition.

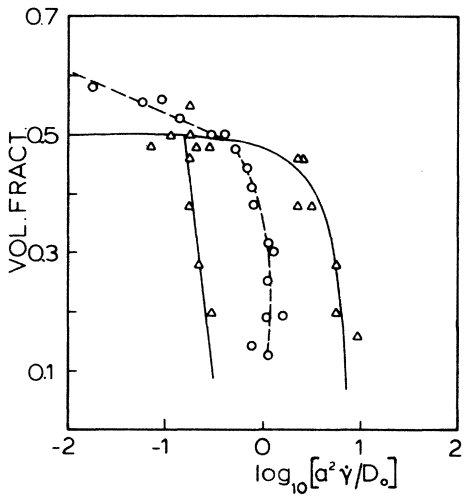

FIG. 6. Phase diagram. Loci of the scattering extrema in Fig. 4 as a function of the Péclet number. Circles are characteristic Peclet numbers obtained from steady shear viscosity measurements (Ref. 42).

IV. DISCUSSION AND CONCLUSIONS

Both Ronis[33] and Hess[34] give forms for the nonequilibrium structure factor $S(\mathbf{k})$, which depends on integrals of the equilibrium static structure factor $S_0(\mathbf{k})$, that apply to arbitrary values of the scattering wave vector and rate of shear. Both results are based on a diffusion equation and neglect hydrodynamic interactions. In Ronis's case a diffusion equation with a $\mathbf{k}$-dependent diffusion constant is treated as a Langevin equation by adding a random force. The random force is assumed to have statistical properties based on the *equilibrium* $S_0(\mathbf{k})$. The shear is introduced via a convective term. $S(\mathbf{k})$ is determined as the $\mathbf{k}$-dependent equal time density correlation function determined from the diffusion-Langevin equation. The result is given as follows:

$$S(\mathbf{k}) = \frac{T}{|k_x|} \int_{k_y k_x/|k_x|}^{\infty} dy (y^2 + k_x^2 + k_z^2) e^{T/|k_x|} \int_{k_y k_x/|k_x|}^{y} dy' (y'^2 + k_x^2 + k_z^2)/S_0(y' k_x k_z) , \tag{4.1}$$

where $T = D_0/2\gamma a^2$. (Note: a is radius, not diameter σ.) In Hess's theory the shear is also introduced through a convective term. An expansion about the equilibrium structure factor is assumed and the diffusion operator is replaced by a single $\mathbf{k}$-independent relaxation rate τ. The relaxation rate is treated as a free parameter. The result is given as follows:

$$S(\mathbf{k}) = \int_0^{\infty} d\alpha\, e^{-\alpha} S_0(k_x, k_y + \alpha T' k_x, k_z) , \tag{4.2}$$

where $T' = \gamma\tau$.

Figures 8 and 9 present the predictions of the Ronis and Hess theories, respectively. In both cases the $S(\mathbf{k})$ is evaluated for $k_{1x}a = \pm 0.46$, $k_{1y}a = 0.49$, $k_{1z}a = 0.0$,

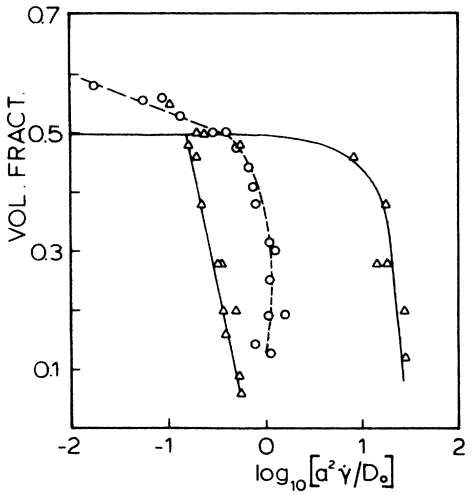

FIG. 7. Phase diagram. Loci of scattering extrema in Fig. 5 as a function of the Péclet number. Circles are characteristic Peclet numbers obtained from steady shear viscosity measurements (Ref. 42).

which corresponds to the data shown in Fig. 4. Since the experimental system is a model hard-sphere system, the Percus-Yevick result[35] for the hard sphere $S_0(\mathbf{k})$ is used in the integration of Eqs. (4.1) and (4.2). The hard-sphere radius is taken to be $a=76$ nm and the volume fractions are as shown in the figure legend. In the Hess theory a choice has to be made for the relaxation rate. The low shear rate expansions of (4.1) and (4.2) are identical if

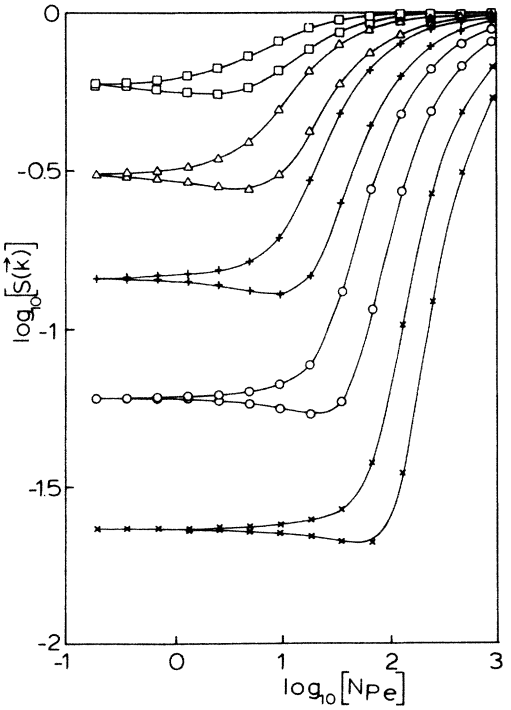

FIG. 8. Theoretical values of $S(\mathbf{k})$ predicted by the theory of Ronis using equilibrium $S_0(\mathbf{k})$ values from the Percus-Yevick theory for hard spheres as a function of the shear rate P_e. The curves are parametrized by volume fractions $\phi=0.1$ (□), 0.2 (△), 0.3 (+), 0.4 (○), and 0.5 (×).

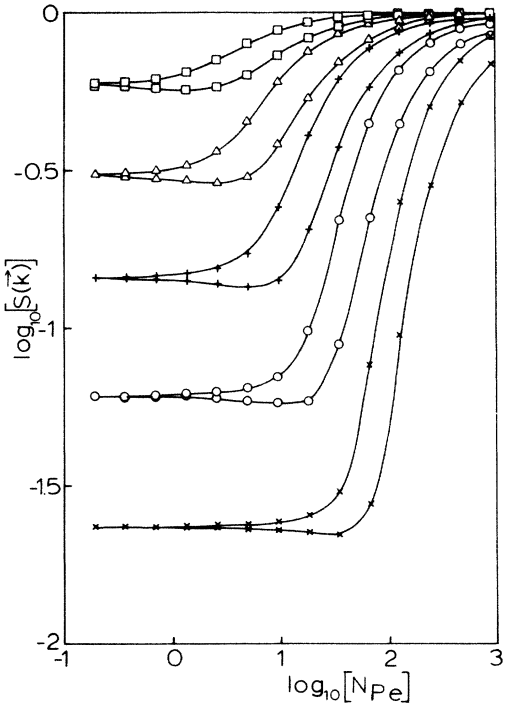

FIG. 9. Theoretical values of $S(\mathbf{k})$ predicted by the theory of Hess using equilibrium $S_0(\mathbf{k})$ values from the Percus-Yevick theory for hard spheres as a function of the shear rate P_e. The relaxation rate is scaled to the Ronis theory, as described in the text. The curves are parametrized by volume fractions $\phi=0.1$ (□), 0.2 (△), 0.3 (+), 0.4 (○), and 0.5 (×).

$\tau=S_0(x)/2D_0x^2$, where x is the experimentally determined value for k. While τ is not assumed to have a $\mathbf{k}$ dependence in relating $g(r)$ to $S(\mathbf{k})$,[34(b)] we assume the aforementioned relationship to make an explicit comparison between the theories of Ronis and Hess at this $\mathbf{k}$ value. In general, however, a single ϕ-dependent, $\mathbf{k}$-independent function for τ should predict values for $S(\mathbf{k})$ for all $\mathbf{k}$ values in Hess's theory.

In Figs. 8 and 9 it can be seen that the two theories are forced to have the same low-shear-rate form. The intensities in this shear-rate range have deviated little from their equilibrium values and this shear-rate independent behavior extends to larger shear rates at larger values of ϕ. The qualitative features of the predictions have many features in common with the experimental data. Both theories give roughly the same order of magnitude effect seen in the data. In both cases the $k_x>0$ and $k_x<0$ intensities split apart at low shear, with the $k_x>0$ branch increasing and the $k_x<0$ decreasing. The $k_x<0$ branch decreases, reaches a minimum, and increases at roughly the same rate as the $k_x>0$ branch. However, there is no decrease in the intensities as the shear rate increases to the largest values.

Ronis developed his theory to compare with experimental results for the very dilute charged particle suspensions of Clark and Ackerson.[29] Here hydrodynamic effects are probably not significant and Ronis's neglect of them is not a bad approximation. In these systems the large particle charge results in high degree of ordering at

low concentration. This ordering reduces the level of scattering at small wave vectors because the collection of particles becomes incompressible and density fluctuations are reduced. Ronis argues that increasing the shear rate disrupts this equilibrium order. The more random positioning of the particles results in an increased scattering at small wave vectors. Thus a disordering process is responsible for the increasing scattered intensity with increasing shear rate. Furthermore, this disordering is delayed to larger shear rates with increasing ϕ in Figs. 8 and 9, because the system becomes more incompressible as ϕ increases. It requires larger shears to disrupt the structure. One might think that the same argument may be made for the increasing intensity region of our hard-sphere data. However, the equilibrium distribution would seem to be the most disordered that hard spheres can be.[47] By definition the particles are placed anywhere in space with equal probability, provided that the particles do not overlap. What then gives rise to the observed increase in intensity? Brady and Bossis[39] have observed distortion of the pair distribution function and particle clustering in suspension dynamics simulations in two-dimensional systems. Such clustering or inhomogeneity could increase forward scattering, given larger scattering at smaller angles. A comparison of our data at k_1 with the data at k_2 shows that the former data have a relatively larger scattering intensity that occurs at a smaller magnitude of the total scattering wave vector. Furthermore, the region where the intensities both increase with increasing shear occurs at shear rates where the Péclet number is order unity, where hydrodynamic effects begin to dominate the Brownian-motion effects.

The phase diagrams presented in Figs. 6 and 7 are qualitatively similar to that suggested by Woodcock. At low volume fractions the two transition lines are shifted to relatively larger shear rates than at larger volume fractions. The phase boundaries intersect at low shear rates at the volume fraction for freezing of hard spheres, suggesting a connection with equilibrium phase properties. The characteristic viscosity is bounded by these two phase boundaries as suggested by Woodcock. Neither the theory of Hess nor Ronis produces a similar phase diagram: There is no maximum intensity predicted by these theories. The phase boundary determined from the intensity minima increases in shear rate with increasing volume fraction. This is contrary to the prediction of Woodcock and the trend of our data. It is not known at this time if the inclusion of hydrodynamic effects in the theories of Ronis or Hess will improve the prediction. We can make an *ad hoc* correction for hydrodynamic effects by replacing the solvent viscosity in Ronis's theory with the low-shear-rate limiting solution viscosity. This correction improves the agreement between theory and experiment but the qualitative behavior remains opposite that of the data.

While the data presented here support the theory of Woodcock in many ways, there are several points to be made. Woodcock views the region at shear rates less than the low-shear-rate phase boundary as a fluid phase. In our case it is a distorted fluid phase. The region between the two phase boundaries is viewed by Woodcock as liquid-phase–smectic-phase coexistence region. If the two phases have different scattering properties, then a mixture of the two phases could produce the increased scattered intensity that we observe. On the other hand, we are reluctant to rule out the formation of clusters as described by Bossis and Brady. In the large-shear-rate region Woodcock claims that a smectic-ordered phase exists. This is consistent with our data if the smectic ordering produces a lesser scattering in the region where we are making measurements. Presumably such structures will produce strong Bragg scattering (from the layers) to wave-vector values larger than is accessible in our experiments using light scattering. However, we do not really know what order exists in this shear-rate region. It could be smectic ordering, string ordering, or something else entirely. Preliminary experiments using larger hard-sphere particles have not yet given clear evidence for smectic or stringlike order at low volume fractions. However, the distortion of the Debye-Scherrer ring has been observed and is consistent with the low-angle data reported here.[48]

The phase transition boundaries determined from our data do not represent sharp first-order transitions as indicated in Woodcock's results. Different scattering angles produce slightly different positions of the phase boundaries. Failure to see sharp first-order transitions may be related to the length scale of our measurements (on the order of ten particle diameters) and will become first order in the limit of forward scattering, $k=0$. On the other hand, the transitions may not be first order at all. The shear field is a symmetry reducing field and the transition from liquidlike order to solidlike order may be via a second-order process, and not contrary to our equilibrium statistical mechanical intuition. We also need to be very clear about what we mean by a phase transition in a nonequilibrium system. Cell boundaries could also produce a transition which appears second order, as ordering may start near a boundary and grow into the bulk. We have ruled out this possibility, as discussed in Sec. II D, by monitoring the scattered intensity at different gap spacings without seeing a quantitative change in behavior.

Future measurements will probe regions in wave-vector space further removed from the origin, near the Debye-Scherrer ring radius. These measurements will be an effort to establish the large-shear-rate structures. The two phase region proposed by Woodcock may exhibit inhomogeneous flow (Hess and Loose[49]) and velocimetry measurements should exhibit anomalous line broadening due to the inhomogeneities. The establishment of sharp phase changes in shearing systems may require long times to develop. Such experiments will be more difficult to perform but should prove interesting. Finally, large volume fraction samples require further investigation to understand the effect of shear on the glass transition and on the solid phase.

ACKNOWLEDGMENTS

One of us (B.J.A.) wishes to thank the University of Utrecht for partially supporting his stay in Utrecht, the

National Science Foundation International Program under Grant No. INT-8521429 for travel and per diem support, and the National Science Foundation, Division of Materials Research, Low Temperature Physics Program, Grant No. DMR-8500704 for partial support. The technical support staff at the Van't Hoff laboratorium are thanked for their high quality and rapid work. Finally, all other staff, faculty, and students are thanked for making his sabbatical stay enjoyable and productive.

---

*Permanent address: Department of Physics, Oklahoma State University, Stillwater, OK 74078.

[1]H. J. M. Hanley, Physics Today **37** (1), 25 (1984); E. G. D. Cohen, *ibid.* **37** (1), 64 (1984); W. G. Hoover, *ibid.* **37** (1), 44 (1984); B. J. Alder and W. E. Alley, *ibid.* **37** (1), 56 (1984).

[2]S. Hess, Physica A **118**, 79 (1983).

[3]W. T. Ashurst and W. G. Hoover, Phys. Rev. A **1**, 658 (1975).

[4]D. J. Evans, Int. J. Thermophys. **7**, 573 (1986).

[5]W. G. Hoover, in *Computer Simulation in Physical Metallurgy,* edited by G. Jaccuci (Reidel, Dordrecht, 1987).

[6]D. Beysens, M. Gbabamassi, and L. Boyer, Phys. Rev. Lett. **43**, 1253 (1979); D. Beysens, in *Scattering Techniques Applied to Supramolecular and Nonequilibrium Systems,* Vol. 93 of *NATO Advanced Study Institute, Series B: Physics,* edited by S. H. Chen, B. Chu, and P. Nossal (Plenum, New York, 1981).

[7]A. Silberberg and W. Kuhn, J. Polymer Sci. **13**, 21 (1954).

[8]S. Hess and H. J. M. Hanley, Phys. Rev. A **25**, 1801 (1982).

[9]S. Hess and H. J. M. Hanley, Thermophysics **4**, 97 (1983).

[10]H. J. M. Hanley and D. J. Evans, Molecul. Phys. **39**, 1039 (1980).

[11]H. J. M. Hanley, D. J. Evans, and S. Hess, J. Chem. Phys. **78**, 1440 (1983).

[12]J. J. Erpenbeck, Phys. Rev. Lett. **52**, 1333 (1984).

[13]L. V. Woodcock, Phys. Rev. Lett. **54**, 1513 (1985).

[14]D. M. Heyes, G. P. Morriss, and D. J. Evans, J. Chem. Phys. **83**, 4760 (1985).

[15]S. Hess, Int. J. Thermophys. **6**, 657 (1985).

[16]D. M. Heyes, J. Chem. Soc. Faraday Trans. **82**, 1365 (1986).

[17]D. J. Evans, H. J. M. Hanley, and S. Hess, Physics Today **37** (1), 26 (1984).

[18]D. J. Evans and G. P. Moriss, Phys. Rev. Lett. **56**, 2172 (1986).

[19]R. L. Hoffman, Trans. Soc. Rheol. **16**, 155 (1972).

[20]R. L. Hoffman, J. Colloid Interface Sci. **46**, 491 (1974).

[21]H. M. Laun, Die Angew. Makromol. Chem. **123**, 335 (1984).

[22]M. Tomita and T. G. M. van de Ven, J. Colloid Interface. Sci. **99**, 374 (1984).

[23]B. J. Ackerson, J. B. Hayter, N. A. Clark, and L. Cotter, J. Chem. Phys. **84**, 2344 (1986).

[24]B. J. Ackerson and N. A. Clark, Phys. Rev. Lett. **46**, 123 (1981).

[25]B. J. Ackerson and N. A. Clark, Physica A **118**, 221 (1983).

[26]B. J. Ackerson and N. A. Clark, Phys. Rev. A **30**, 906 (1984).

[27]I. M. Krieger, Adv. Colloid Interface Sci. **3**, 111 (1972).

[28]M. Lindsay and P. M. Chaikin, J. Phys. (Paris) **46**, C3-269 (1983).

[29]N. A. Clark and B. J. Ackerson, Phys. Rev. Lett. **44**, 1005 (1980).

[30]D. M. Husband and F. Gadala-Maria, J. Rheol. **31**, 95 (1987).

[31]C. W. J. Beenakker and P. Mazur, Phys. Lett. **98A**, 22 (1983).

[32]P. Mazur and W. van Saarloos, Physica A **115**, 21 (1982); W. van Saarloos and P. Mazur, *ibid.* **120**, 77 (1983).

[33](a) D. Ronis, Phys. Rev. Lett. **52**, 473 (1984); (b) Phys. Rev. A **29**, 1453 (1984).

[34](a) S. Hess, Phys. Rev. A **22**, 2844 (1980); (b) J. F. Schwarzl and S. Hess, *ibid.* **33**, 4277 (1986).

[35]P. A. Egelstaff, *Introduction to the Liquid State* (Academic, London, 1967).

[36]G. K. Batchelor, J. Fluid Mech. **83**, 97 (1977).

[37]W. B. Russel and A. P. Gast, J. Chem. Phys. **84**, 1815 (1986).

[38]L. V. Woodcock, Chem. Phys. Lett. **10**, 257 (1971).

[39]G. Bossis and J. F. Brady, J. Chem. Phys. **80**, 5141 (1984).

[40]P. De Gennes, J. Phys. (Paris) **40**, 783 (1979).

[41]J. Mellema, C. G. de Kruif, C. Blom, and A. Vrij, Rheol. Acta **26**, 40 (1987).

[42]C. G. de Kruif, E. M. F. van Iersel, A. Vrij, and W. B. Russel, J. Chem. Phys. **83**, 4717 (1985).

[43]A. K. van Helden, J. W. Jansen, and A. Vrij, J. Colloid Interface Sci. **81**, 354 (1984).

[44]A. Vrij, J. W. Jansen, J. K. G. Dhont, C. Pathmamanoharan, M. M. Kops-Werkhoven, and H. M. Fijnaut, Faraday Disc. Chem. Soc. **76**, 19 (1983).

[45]C. G. de Kruif, J. W. Jansen, and A. Vrij, in *Complex and Supramolecular Fluids,* edited by S. Safran and N. Clark (Wiley, New York, 1987).

[46]C. G. de Kruif, W. J. Briels, R. P. May, and A. Vrij, Langmuir (to be published).

[47]It may be argued that more random distributions do exist, such as random packing [L. V. Woodcock (private communication)].

[48]B. J. Ackerson and P. N. Pusey (unpublished).

[49]S. Hess and W. Loose (private communication).